Centauro And STrange Object Research

CASTOR

A.L.S. Angelis[1], S.N. Filippov[2],
E. Gladysz-Dziadus[3], Yu.V. Kharlov[4], A.B. Kurepin[2],
A.D. Panagiotou[1] and S.A. Sadovsky[4]

[1] Nuclear and Particle Physics Division, Department of Physics, University of Athens.
[2] Institute for Nuclear Research, Russian Academy of Sciences, Moscow.
[3] Institute of Nuclear Physics, Department of High Energy Physics, Cracow.
[4] Institute for High Energy Physics, Protvino.

A DETECTOR FOR ALICE AT VERY FORWARD RAPIDITY DEDICATED TO THE IDENTIFICATION AND STUDY OF 'CENTAUROS' AND 'STRANGELETS'

TECHNICAL PROPOSAL
(CURRENT STATUS REPORT)

Contents

1 INTRODUCTION

The physics motivation to study the very forward phase space in nucleus–nucleus collisions is based on the potentially very rich field of yet undiscovered novel phenomena, produced in and by an environment with extremely high baryochemical potential. The study of the extreme baryon-dense state (much denser than the highest baryon density produced at the AGS or SPS), formed in the Lorentz-contracted and collision-compressed receding 'nuclear pancake', may provide necessary (and in no other way available) information for the understanding of a Deconfined Quark Matter (DQM) state at relatively low temperature, thought to exist in the core of neutron stars.

In addition, cosmic-ray experiments have detected numerous most unusual events, whose nature is still not understood. These events, observed in the projectile fragmentation rapidity, may be produced and studied in controlled accelerator experiments at the LHC.

It is also important that at least one LHC experiment looks at what may happen in the very forward part of phase space. This is especially interesting, given suggestions from theory that other important new phenomena are likely to occur at these energies in the forward directions [1]. Searching for unusual or unexpected phenomena may turn out to yield a new understanding of high-energy strong interactions.

Our first basic experimental aim is to identify events with characteristics similar to those of the 'exotic' cosmic-ray collisions, in central $Pb + Pb$ interactions at very forward rapidity, in an event-by-event mode. We will look for:
- low charged particle multiplicity compared with normal hadronic interactions;
- extreme imbalance between the hadronic and photonic components, both in terms of the particle multiplicity and the energy content of the event;
- non-uniform (in ϕ) deposition of a large amount of energy;
- highly penetrating objects, far beyond the range of normal hadrons.

The baseline detector system we propose should be able to identify such events. If this is achieved, the detailed study of this type of 'exotic' event and the identification of particles associated with them will require small modifications and/or additions to the detector.

2   PHYSICS

2.1   Motivation

Cosmic-ray experiments have shown the existence of very peculiar events, which defy the known hadronic nature [2]. Classes of these events, the so-called 'Centauro' and 'Chiron', exhibit very small multiplicity, complete absence (or strong suppression) of the electromagnetic component and extremely high $\langle p_{\mathrm{T}} \rangle \sim 1.7$ and 2–3 GeV/c, respectively. In addition, many hadron-rich events possess a long-flying (hadronic) component, i.e. abnormally long-penetrating particles. It was shown by Monte Carlo (MC) simulations [3] that these events could not originate from any kind of rare statistical fluctuations of normal hadronic interactions.

Several models have been proposed to describe the nature of the Centauro events, some amenable to experimental verification and some not. Among the former, the diffractive dissociation of a fireball in p–p collisions [4] and the production and decay of the η_6 (quark sextet) particle [5] have not given positive results so far. Another model [6] considers these events to originate from the hadronization of a DQM fireball [7], produced in nucleus–nucleus collisions in the upper atmosphere. In this model, both the extreme imbalance of the hadronic to photonic content of the Centauro event and possibly the strongly penetrating particles, considered to be strangelets, are naturally explained. Centauros and strangelets are thought to be the products of hadronization of a DQM state with very high density ($\rho > 2$ fm^{-3}) and baryochemical potential ($\mu_{\mathrm{b}} > \mathrm{m_n}$).

The development of the Centauro fireball is summarized below [6].

- Formation of a DQM fireball.

  The DQM fireball is created in the baryon-rich projectile fragmentation region. Initially, it consists of u,d quarks and gluons. The very high baryochemical potential prohibits the creation of u$\bar{\mathrm{u}}$ and d$\bar{\mathrm{d}}$ quarks (Pauli blocking of u,d quarks and the factor $\exp\left(-\mu_{\mathrm{q}}/\mathrm{T}\right)$ for antiquarks), resulting in the fragmentation of gluons into s$\bar{\mathrm{s}}$ only. This causes the total suppression of pions and hence of gammas, if isospin is to be conserved. The fireball's very high matter density (high binding energy) and relatively low temperature may extend its lifetime to $\tau_0 > 10^{-22}$ s.

- Chemical equilibrium.

  A state of (partial) chemical equilibrium may be approached in a time interval $\sim 10^{-23}$ s, the relaxation time for g $\rightarrow$ s$\bar{\mathrm{s}}$. During this time several K$^+$($\bar{\mathrm{s}}$u) and K^0($\bar{\mathrm{s}}$d) are emitted, carrying away strange antiquarks, positive charge, entropy and lowering further the temperature.

- Strange quark-matter state.

  After emitting kaons, the DQM fireball becomes a mixture of u, d and s quarks. In the absence of u and d antiquarks, s quarks are unable to hadronize quickly by emitting anti-kaons. This results in the presence of net strangeness and the transformation of the initially quark-matter fireball into a slightly *strange quark-matter* state. The finite excess of s quarks and their stabilizing effects transform the Centauro fireball into a long-lived state, stable against strong interactions, with $\tau_{\mathrm{cnt}}^0 > 10^{-13}$ s able to reach mountain-top altitudes.

- Hadronization.

  A mechanism of strangeness separation [8] can cause the strange quark content of the Centauro fireball to form low-mass strangelet(s). The fireball finally decays into non-strange baryons and long-lived [6, 9] strangelet(s), which have a very high strangeness-to-baryon ratio ($\mathrm{f_s} = \mathrm{N_s}/\mathrm{A} \sim 1$), very low charge-to-baryon ratio

$(Z/A \leq 0)$, and small mass $(A_{str} \sim 7\text{–}15)$. They could be identified as the highly penetrating particles, frequently accompanying the hadron-rich cosmic-ray events.

Our proposal to identify and study Centauro-type events and the co-produced strongly penetrating 'hadrons', considered to be strangelets, with the detector system 'CASTOR' is based on this model [6].

2.2 Cosmic-ray Centauros and strangelets

The analysis of lateral distributions of cosmic-ray Centauros has shown that the hadrons are observed at average pseudorapidity $\langle \eta_{cnt} \rangle = 9.9 \pm 0.2$. Assuming that they are produced in 'Fe + N' collisions at $\langle E_{lab} \rangle \sim 1740$ TeV, the projectile rapidity is $\langle y_{pr}^{lab} \rangle \sim 11$. Thus, Centauros are produced in the projectile fragmentation region. The cross-section for Centauro events is of O(1%). Table 2-1 summarizes the (average) experimental and estimated characteristic quantities of cosmic-ray Centauros and strangelets [6].

A Centauro fireball must have at least a lifetime $\tau_{cnt}^0 > O(10^{-13}$ s) in its own rest frame, corresponding to $\tau = \gamma \; \tau_{cnt}^0 = \cosh y_{cnt} \; \tau_{cnt}^0 \sim O(10^{-9}$ s) in the lab frame, in order to reach mountain-top level. If the Centauro fireball decays, say 500 m above the detector, and the long-flying component is identified with strangelets, a strangelet with mass 10 GeV must have a lifetime of at least $O(10^{-6}$ s), $\tau_{str}^0 > O(10^{-10}$ s), to go through the detector.

The very penetrating component among the hadronic showers is an astonishing evidence for abnormal hadronic interaction or a new kind of hadron 'species'. Figure 2.1 shows the multiplicity versus energy characteristics of a Centauro-type event of total visible energy of 690 TeV [10] among the known (mini)Centauro and normal hadronic events. The very hadron-rich nature of this event is evident. Figure 2.2 shows the typical shower transition curves of the very penetrating objects in hadron-rich cosmic-ray events [10, 11], as a function of the absorber depth.
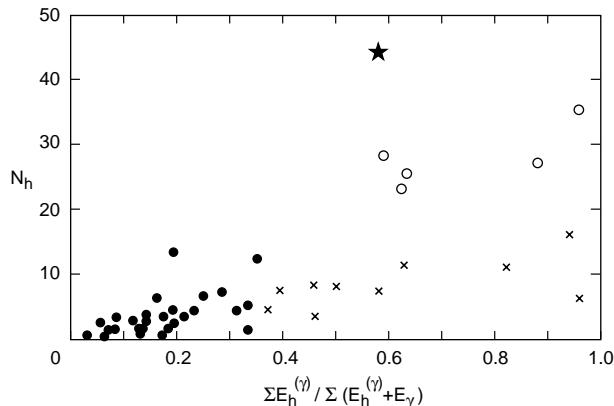

Figure 2.1: Number of hadrons N_h vs. energy fraction of hadronic component. Chacaltaya families with total energy ≥ 100 TeV: o Centauro-type; x mini-Centauro-type; • normal events; ⋆ Centauro-like event (reprinted from ref. [10]).

In the first event [10], there are two such very penetrating hadron cascades (upper two transition curves). One 'hadron', with total visible energy of ~ 170 TeV, starts cascading at a depth of 12 c.u. and after passing 109 c.u. of lead (61 cm, 3.6 λ_I) escapes unattenuated through the bottom of the chamber. The other, with 102 TeV total visible energy, starts cascading at 48 c.u. and escapes unattenuated through the bottom of the

chamber, having traversed 72.4 c.u. (40.5 cm, 2.4 λ_I). The longitudinal structure of their transmission curves is clearly visible, exhibiting 11 and 5 maxima, respectively (with an average distance of 10.5 ± 4 c.u.), which are satisfactorily fitted by individual EM curves.

In the lower event [11], the shower starts developing at 14 c.u. and persists unattenuated down to the bottom of the chamber, having traversed 97 c.u. of lead (48 cm, 2.8 λ_I). The total visible energy of this hadron is ~ 177 TeV. Note that, imposing the same energy threshold as in this analysis, the cascade of a normal hadron of equal energy extends only about 46 c.u. (25.8 cm, 1.5 λ_I) in lead, starting after about 3–5 c.u., whilst the distance between maxima is $\sim 23 \pm 10$ c.u. Note also that in hadron-rich events, occasionally more than one such very penetrating 'hadrons' have been observed.
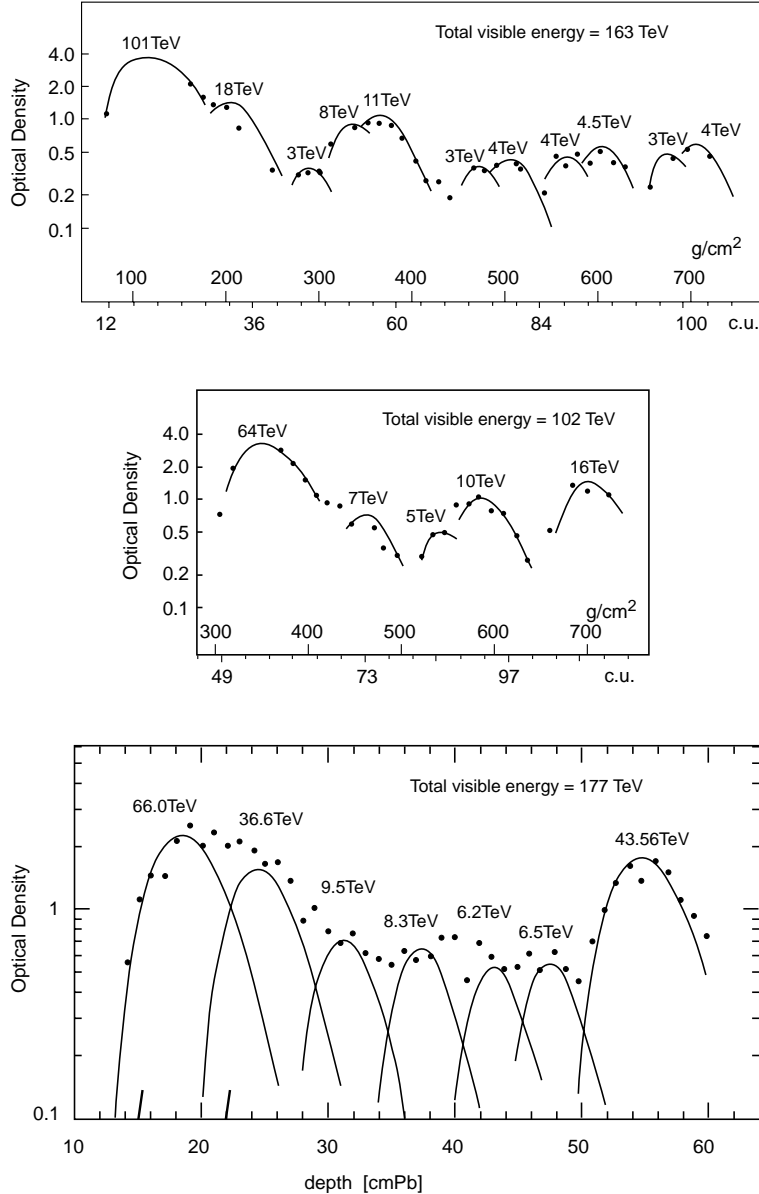

Figure 2.2: Transition curves of long-range cascades with many maxima, observed in the multilayer lead chambers. The amount of energy liberated into the soft component is indicated at each hump. (a) and (b) from the Centauro-like family [10], (c) from event of ref. [11].

6

Table 2-1

Centauro fireball

Hadron multiplicity	$\langle N \rangle \sim 64\text{--}90, \langle 75 \rangle$
Gamma multiplicity	~ 0
Average total incident energy	$\langle E_{cnt} \rangle \geq 1740$ TeV
Total interaction energy in '60+14' c.m.	$\sqrt{s} \geq 6760$ GeV
Total interaction energy in N–N c.m.	$\sqrt{s}_{N-N} \leq 233$ GeV
Incident nucleus rapidity in laboratory frame	$y_{pr} \sim 11.03$
Midrapidity of '60+14' system	$y_{c.m} \sim 6.24$
Laboratory pseudorapidity of emitted baryons	$\langle \eta_{cnt} \rangle \sim 9.9 \pm 0.2$
Width of pseudorapidity distribution	$\langle \Delta\eta_{cnt} \rangle \sim 1 \pm 0.2$
Average transverse momentum	$\langle p_T \rangle \sim 1.75 \pm 0.7$ GeV/c
Mass of fireball	$M_{fb} \sim 180 \pm 60$ GeV
Volume of fireball	$V_{fb} \sim 75\text{--}100$ fm^3
Energy density of fireball	$\varepsilon_{fb} \sim 2.4 \pm 1$ GeV fm^{-3}
Baryochemical potential of fireball	$\mu_b \sim 1.8 \pm 0.3$ GeV
Temperature of fireball	$T_{fb} \sim 130 \pm 6$ MeV
Quark density of fireball	$\rho_q \sim 8 \pm 3$ fm^{-3}
Baryon density of fireball	$\rho_b \sim 2.7 \pm 1$ fm^{-3}
Strange-quark density	$\rho_s \sim 0.14$ fm^{-3}
Antiquark density	$\rho_{\bar{q}} \sim 3.6 \times 10^{-3}$ fm^{-3}
Gluon density	$\rho_g \sim 0.6$ fm^{-3}
Entropy density	$S \sim 16.4$ fm^{-3}
Entropy/baryon density	$S_b \sim 6$
Strangeness/baryon density	$\rho_s/\rho_b \sim 0.06$
Net strangeness	$N_s - N_{\bar{s}} \sim 14$
Final charge/baryon	$(Z/A)_f \sim 0.4$
Lifetime	$\tau_{cnt}^0 > O(10^{-9}$ s$)$

Centauro strangelet(s)

Mass	$A \sim 7\text{--}15$
Charge/baryon	$Z/A \leq 0$
Strangeness/baryon	$f_s \sim 1$
Lifetime	$\tau_{str}^0 > O(10^{-10}$ s$)$

Figure 2.3 shows the distribution of shower-starting positions of the very penetrating hadrons in the chamber material, measured by λ(geo). The numbers in parentheses indicate the multitude of such particles, observed in different chambers (detectors). The experimental observations show the collision mean free path for these highly penetrating particles (solid line) to be very small, about 1/2–1/3 of the hadronic geometrical value observed in ordinary cosmic-ray hadrons (dashed line). Moreover, this observation is opposite to the expectation, based on the inelasticity coefficients for collisions of ordinary hadrons and of hadrons from 'exotic' events.

The question of a possible connection between the strongly penetrating component and strangelets is being investigated [33]. To check this hypothesis we have considered several possible decay [34] and interaction [35] modes of a light strangelet and we have simulated its traversal through the homogenous thick lead chamber. We have examined

unstable (decaying in the timescales typical for strong processes $\tau_0 \leq 10^{-20}$ s), metastable (decaying within a lifetime $\tau_0 \leq 10^{-4}$ s) and stable strangelets. Our preliminary calculations show that in all cases it is possible to obtain through the simulation transition curves resembling the experimental ones. The 'stable' strangelet, traversing the chamber without decaying, can produce the successive humps in the process of its interactions with the absorber nuclei. The example of a typical cascade curve, produced by the unstable strangelet, evaporating N=7 neutrons is shown in Fig. 2.4.
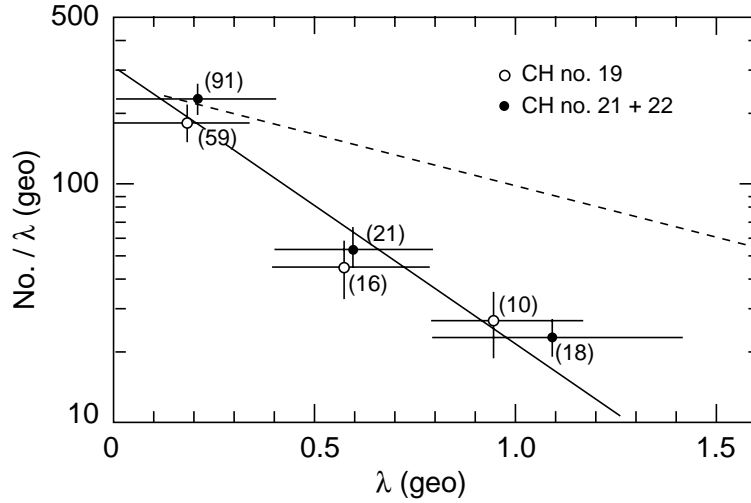

Figure 2.3: Distribution of shower starting positions for high energy hadrons associated with chiron-type families, the broken line shows the attenuation for ordinary hadrons (reprinted from ref. [11]).
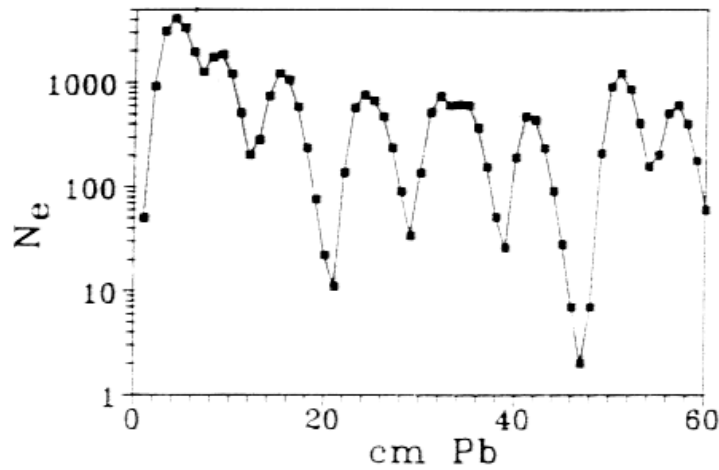

Figure 2.4: Example of simulated transition curve produced by an unstable strangelet, decaying into N=7 neutrons, recorded in emulsion chamber with the lead absorber ($E_s$tr = 200 TeV/baryon).

8

2.3 Centauros and strangelets at the LHC

A DQM state may be formed within the colliding Pb nuclei after interpenetration. The 'nuclear transparency' at LHC energies ensures strong concentration (in rapidity) of the baryon number density, within the receding nuclear fireball, shown schematically in Fig. 2.5. HIJING and VENUS event generators show that the baryon number density is contained within ~ 2 units of rapidity, at y ~ 6.8 and y ~ 5.9 respectively (Fig. 2.6 for VENUS), indicating a rapidity shift due to nuclear stopping of 1.87 and 2.77, respectively.
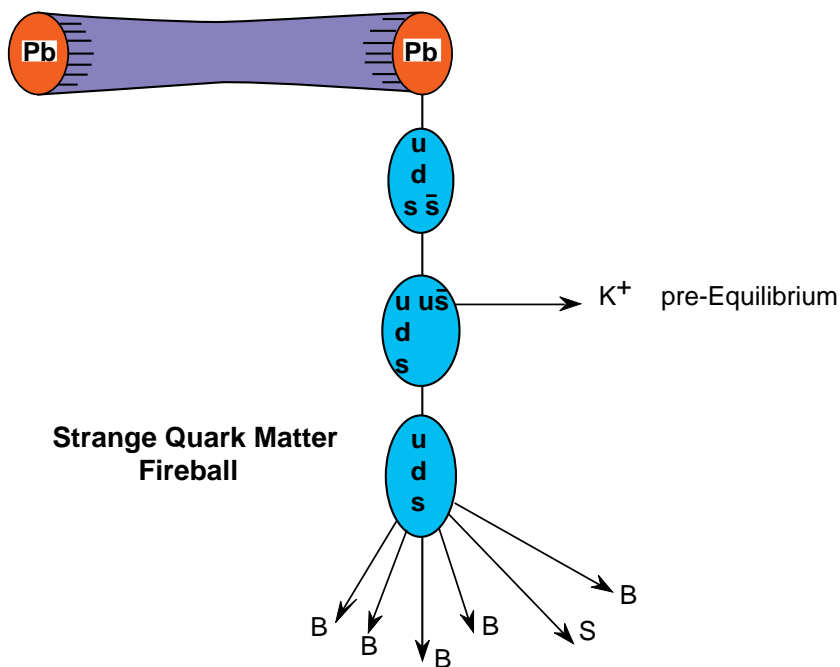
Figure 2.5: Schematic representation of the formation and decay in $Pb + Pb$ interactions of a strange quark matter fireball.
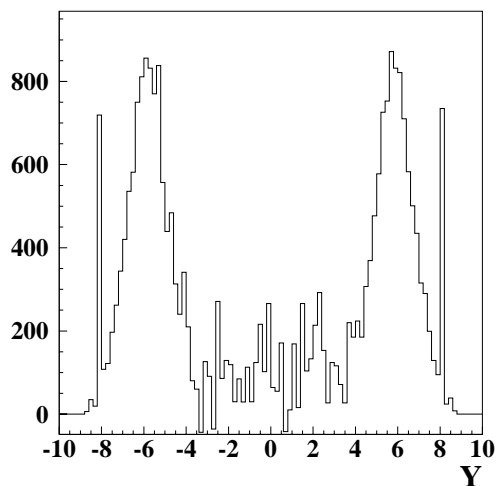
Figure 2.6: Net baryon number rapidity distribution obtained from 47 central $Pb + Pb$ Venus events.

This also indicates the extent of the baryon-free midrapidity, which reaches up to rapidity y $\sim$ 4. Therefore, according to our model of a Centauro event, above y $\sim$ 4 we expect to find only the fragmentation of the baryonic fireball producing the Centauro event, without pions, photons or antiparticles. The produced background will, of course, alter somewhat this ideal situation (see discussion in Section 5).

In very central $Pb + Pb$ interactions at the LHC, the Centauro fireball may have a mass,

$$\langle M_c \rangle = \langle N_p \rangle \langle E_n \rangle = \langle N_p \rangle \sqrt{[(4\langle p_T \rangle / \pi)^2 + m_n^2]} \sim O(450 \text{ GeV}) \;,$$

where $\langle N_p \rangle \sim 190$ is the number of participant nucleons per nucleus and $\langle p_T \rangle \sim 1.7 \text{ GeV}/c$, as in the cosmic-ray Centauro. The gamma (Lorentz factor) is $\gamma = \cosh{(y_{\text{beam}} - \Delta y_{\text{n.s.}})} \sim \cosh{(6.4)} \sim 300$, where $\Delta y_{\text{n.s.}} \sim 2.3$ is the average rapidity shift due to nuclear stopping, predicted by the two event generators. The total energy of the Centauro fireball is then, $E_c = \gamma M_c \sim O(130 \text{ TeV})$. For order of magnitude calculations, we take the longitudinal momentum $p_L \sim E_c$ and estimate a minimum lifetime $\tau_c \sim O(10^{-6} \text{ s})$, $\tau_c^0 \sim O(10^{-9} \text{ s})$, for the fireball to reach the detector before decaying. It is therefore uncertain, but not improbable, that Centauro fireballs will reach the detector located about 11 m away and decay inside. If this does happen, we may see the deposition of a very large amount of energy in a small phase space.

To carry out an estimation for a strangelet, we assume that it has the same gamma factor as the Centauro fireball and a mass of $O(10 \text{ GeV})$. Taking again $p_L \sim E_s = \gamma M_s \sim 3 \text{ TeV}$, the lifetime necessary to reach and go through the detector is $\tau_s \sim O(10^{-7} \text{ s})$, $\tau_s^0 \sim O(10^{-10} \text{ s})$. If strangelets are unstable against strong interactions $[\tau_s^0 \sim O(10^{-20} \text{ s})]$, they will decay immediately after the Centauro fireball decay. One will, in this case, observe a strongly 'collimated' bundle of hadrons (mostly neutrons), with small relative p_T, penetrating deeply into the detector. If, on the other hand, strangelets are metastable states $[\tau_s^0 \sim O(10^{-4} \text{ s})]$ [9], they will reach and go through the detector and may be seen as a highly penetrating 'hadron'. In both cases the picture observed in the calorimeter will be different than that in the case of passage of 'normal' hadrons [33] and will resemble the long-lived many-maxima cascades known from cosmic ray experiments. A calorimeter with the capability to sample the development and propagation of hadronic showers along its depth is the necessary detector for such observations.

2.3.1 Hadron multiplicity

To calculate the expected multiplicity of hadrons (baryons) from the decay of the Centauro fireball, formed in central $Pb + Pb$ interactions, we make the following assumptions and estimations [6]:

– Number of participant nucleons: $\langle N_p \rangle \leq 190$ (per interacting nucleus)
– Volume of fireball: $V \leq \pi (1.1 \times 190^{1/3})^2 \times 1 \sim 125 \text{ fm}^3$
– Temperature of fireball: $T \leq 190 \text{ MeV}$
– Strange-quark density: $\rho_s \leq 0.5 \text{ fm}^{-3}$
– Number of strange quarks: $\langle N_{s,\bar{s}} \rangle \leq 125 \times 0.5 \sim 60$
– Number of emitted kaons: $\langle K^+ + K^0 \rangle \leq 60$

Assuming in addition that all s quarks form strangelets (an extreme scenario) with $f_s = N_s/A \sim 1$, $Z/A \leq 0$, we estimate that a maximum of 4–8 strangelets with mass $\sim$ 15A–7A, respectively, will be emitted. About 130 baryons will also be emitted to conserve the baryon number of the fireball. The approximately 60 kaons are emitted at the very early stage of the fireball and probably with less transverse momentum ($p_T \sim 0.5 \text{ GeV}/c$).

It should be noted that these multiplicities for the strangelets are upper limits. If the temperature of the Centauro fireball is lower, the number of s$\bar{s}$ quarks decreases and the final baryon multiplicity increases. Thus, our calculations are for two limiting multiplicities of 130 and 160 for the decay baryons.

2.3.2 Hadron rapidity distribution and CASTOR acceptance

The rapidity distribution expected for the Centauro decay products at LHC is calculated, assuming a $\langle p_T \rangle \sim 1.7$ GeV/c and a mean nuclear stopping of about 2.3 units of rapidity (average of HIJING & VENUS predictions):

$$y_c^{decay} = y_{beam} - \Delta y_{n.s.} - \Delta y_{p_T} \sim 8.67 - 2.32 - 0.9 \sim 5.45 \pm 1 . \tag{1}$$

The integral spectrum of hadrons emitted from the cosmic-ray Centauro fireball can be approximated by an exponential function of the fractional energy, $f = E_n/E_c$:

$$N_n(f > E_n/E_c) = N_c \exp \left[-N_c(E_n/E_c) \right] \tag{2}$$

where E_n is the energy of the hadron and E_c the total energy of the Centauro interaction. N_c is the total multiplicity of hadrons (baryons) emitted from a Centauro fireball.

The shape of the spectrum is the result of the isotropic emission of particles from a fireball with a Planck type momentum distribution. Assuming the same behaviour for the LHC Centauro as for the cosmic-ray ones, the resulting spectrum of hadrons for $N_c = 130$ and 160 is shown in Fig. 2.7. The region corresponding to the acceptance of the CASTOR detector is also shown. The threshold values for the fractional energy, $f_{th} = E_n^{th}/E_c$, have been calculated using

$$E_n^{th} = m_T \cosh y_{th} = \sqrt{(p_{Tn^2} + m_n^2)} \cosh y_{th} \tag{3}$$

and

$$E_c = M_c \cosh (y_{beam} - \Delta y_{n.s.}) = N_p m_n \cosh (y_{beam} - \Delta y_{n.s.}) \tag{4}$$

The marked region has been obtained for $\Delta y_{n.s.} = 2.3$. For such values of parameters, we accept in the detector ($y_{th2} = 4.5$, $y_{th1} = 6.2$) about 60% of the produced particles:

$$A \sim \exp \left[-N_n m_T \cosh y_{th1}/N_p m_n \cosh (y_{beam} - \Delta y_{n.s.}] \right.$$

$$-\exp \left[-N_n m_T \cosh y_{th2}/N_p m_n \cosh (y_{beam} - \Delta y_{n.s.}] \right. \tag{5}$$

The dependence of the acceptance A on the value of the rapidity shift due to nuclear stopping is shown in fig. 2.8 for the fireball decay baryons.
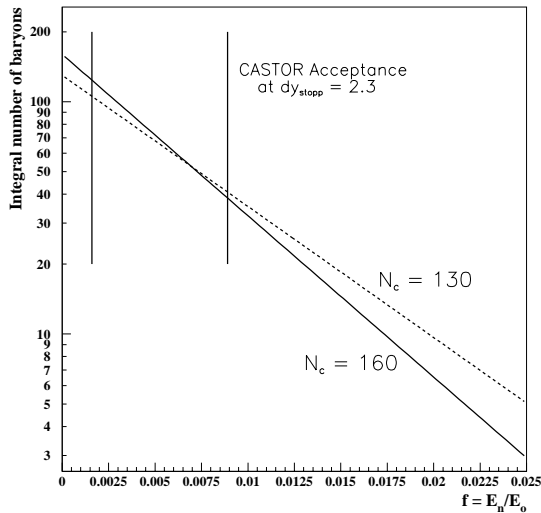
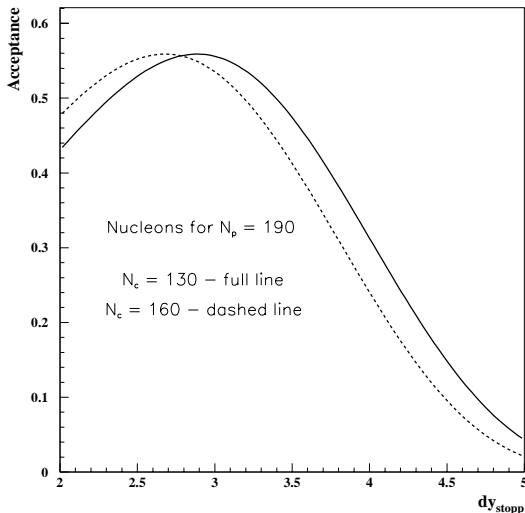Figure 2.7: Integral fractional energy spectrum of baryons emitted from a Centauro fireball (see text).

Figure 2.8: Geometrical acceptance of CASTOR as a function of the value of the rapidity shift due to nuclear stopping.

2.3.3 Centauro event generator

According to our model, in ultra-relativistic central nucleus–nucleus collisions the Centauro event is formed by the DQM state within the baryonic fireball of the receding nucleus. This state consists of only constituent u,d quarks and created $s\bar{s}$ quarks. It decays only to baryons and strangelets, with total absence (or strong suppression) of all pions. Therefore, in the rapidity range where the baryon-number density appears ($\sim 4.0 < y < 8$) there will be only baryons (non-strange and strange) and K^+, K^0.

We have 'constructed' the rapidity distribution of particles emitted from Centauro events by taking normal events produced by an event generator, in this case HIJING, and imposing the following restrictions:

- At $|y| < 4$, admit all particles produced in a 'normal' event.
- At $|y| \geq 4$, admit only particles produced from 'constituent' u,d and $s\bar{s}$ quarks:
$$(p - \bar{p}), (n - \bar{n}), (K^+ - K^-),$$
$$(\Lambda - \bar{\Lambda}), [(\Sigma^0, \Sigma^+, \Sigma^-) - (\bar{\Sigma}^0, \bar{\Sigma}^+, \bar{\Sigma}^-)]$$
$$[(\Xi^0, \Xi^-) - (\bar{\Xi}^0, \Xi^+)], \Omega^-, \Omega^+ .$$
- Forbid all directly produced, light, unflavoured mesons (requiring light antiquarks for hadronization).

Figure 2.9 shows the expected rapidity distribution of hadrons produced in a normal event (a) and in a Centauro event (c), as prescribed above. Figure 2.9b shows the baryon-number rapidity distribution.

A Monte Carlo code for the formation of Centauro fireballs in $Pb + Pb$ interactions at $\sqrt{s} = 2.77$ TeV/nucleon is currently being developed [12]. It is based on the model of reference [6] and takes into account different impact parameters, baryochemical potentials, temperatures and the dynamics of the Centauro fireball. It gives distributions of: the fireball mass (Fig. 2.10); the transverse momentum of the fireball decay hadrons (Fig. 2.11); the rapidity distribution of the decay hadrons (Fig. 2.12); their multiplicity as seen by the charged-particle multiplicity detector (Fig. 2.13 and 2.14) and the ratio of

the hadronic to the total multiplicity and energy (Fig. 2.15 and 2.16). Although the code is in its initial development stage, it is useful for semi-quantitative arguments.
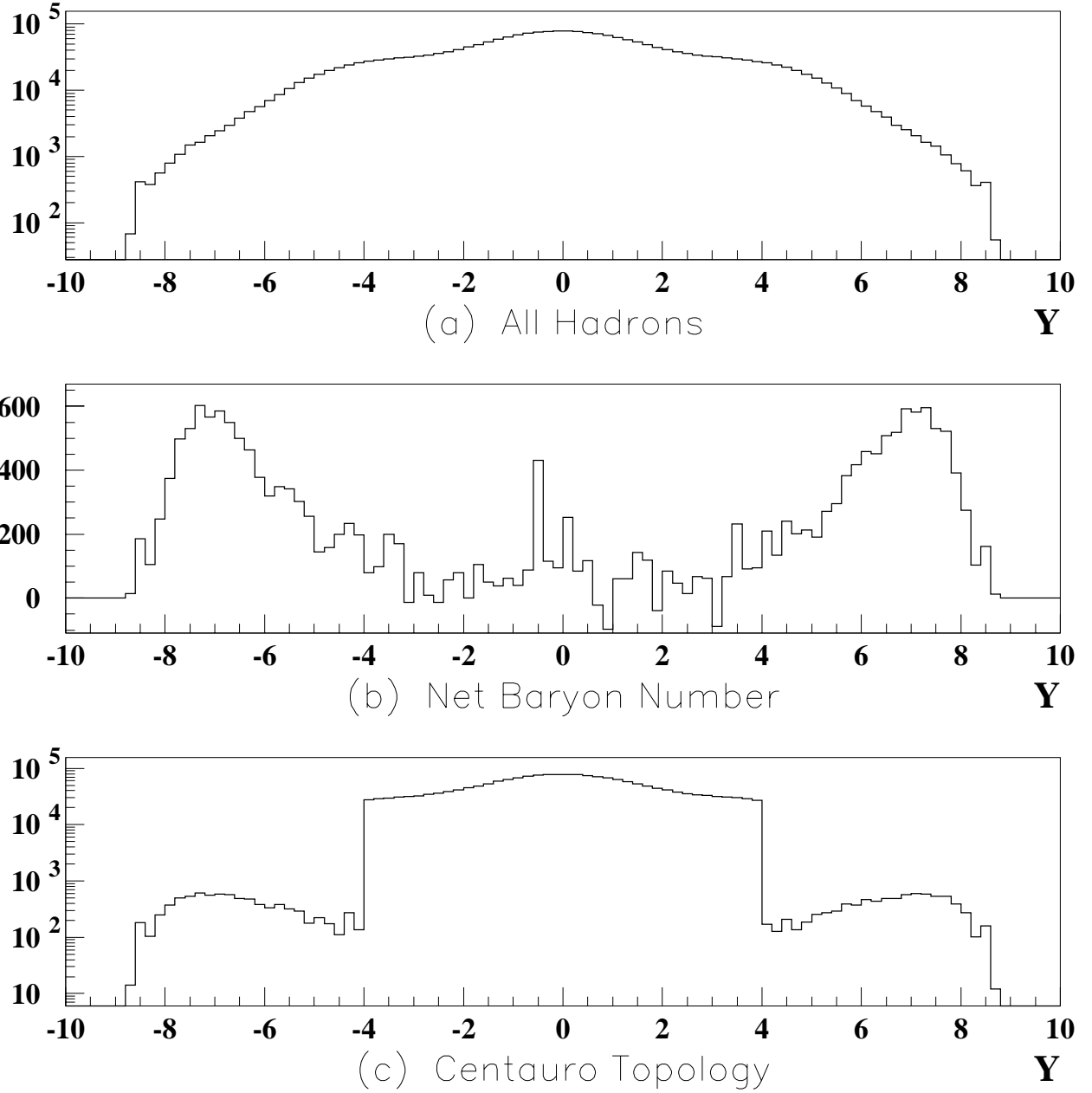

Figure 2.9: Simulation of rapidity distribution in a $Pb+Pb$ collision resulting in a Centauro event, obtained from 50 central $Pb + Pb$ HIJING events (see text): (a) hadron distribution in a normal event, (b) net baryon number distribution, (c) hadron distribution in a Centauro event.
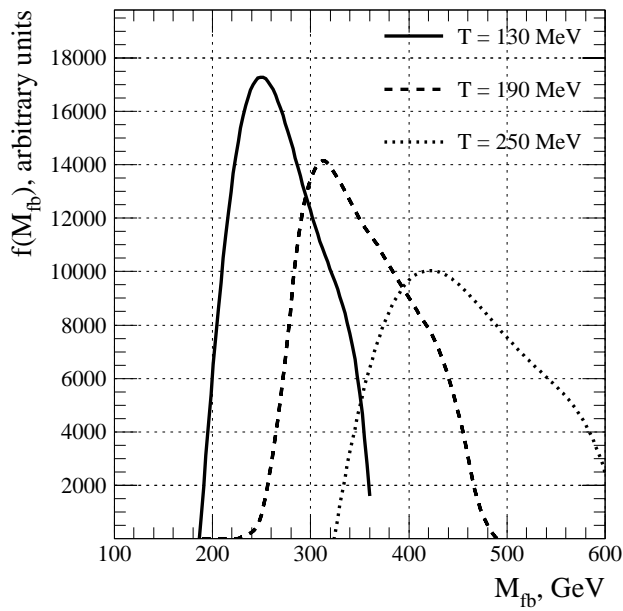
13

Figure 2.10: Mass of the Centauro fireball in $Pb + Pb$ collisions at $\mu_b = 1.8$ GeV and $T = 130$, 190 and 250 MeV.
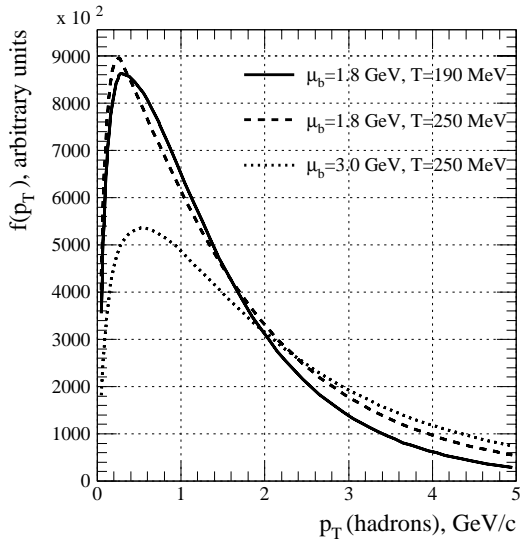

Figure 2.11: Transverse momentum distribution of hadrons in Centauro event with ($\mu = 1.8$ GeV, $T = 130$ MeV), ($\mu = 1.8$ GeV, $T = 190$ MeV) and ($\mu = 3.0$ GeV, $T = 250$ MeV).
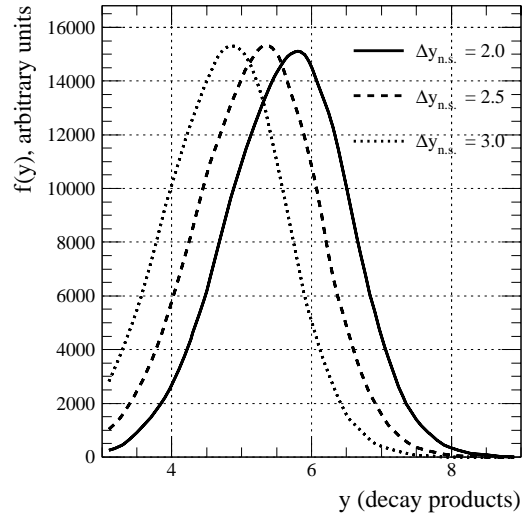
Figure 2.12: Rapidity distribution of decay products of Centauro events for three values of $\Delta y_{\mathrm{n.s.}} = 2.0$, 2.5 and 3.0.

14
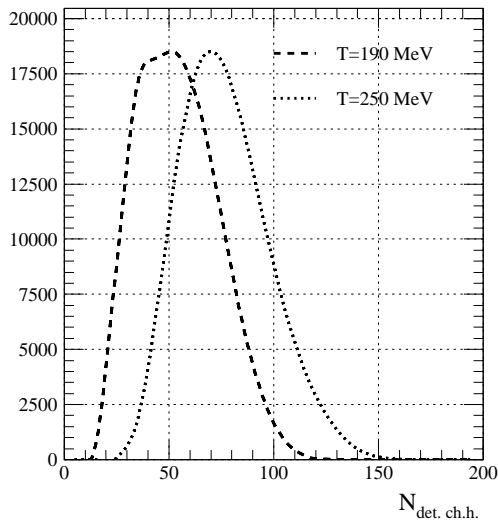
Figure 2.13: Charged hadron multiplicity in the detector at $\Delta y_{\mathrm{n.s.}} = 2.5$, $\mu = 1.8$ GeV and two values of $T = 190$ and 250 MeV.

Figure 2.14: Charged hadron multiplicity in the detector at $\mu = 1.8$ GeV, $T = 250$ and three values of $\Delta y_{\mathrm{n.s.}} = 2.0$, 2.5 and 3.0.

Figure 2.15: Ratio of hadron to total multiplicity (hadrons + photons).

Figure 2.16: Ratio of hadronic to total energy.

3   THE CASTOR SUB-DETECTORS

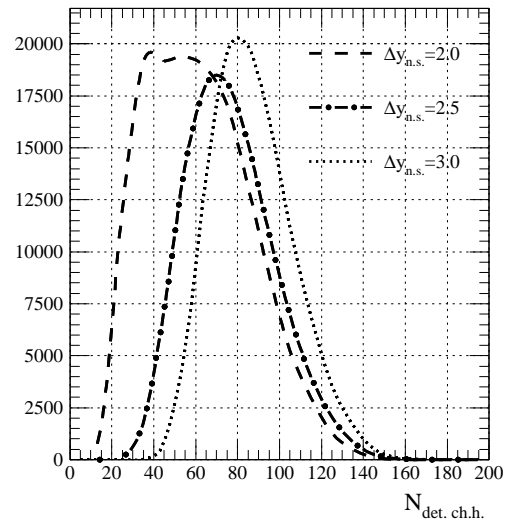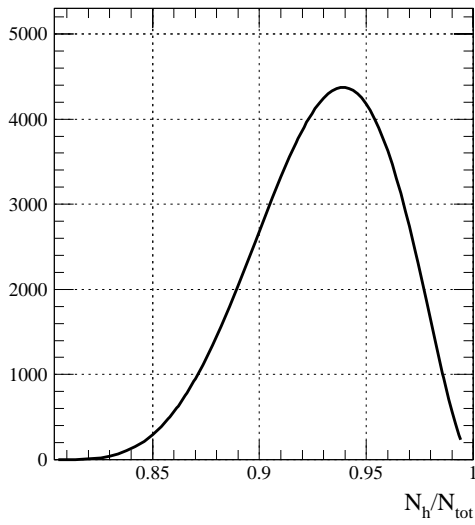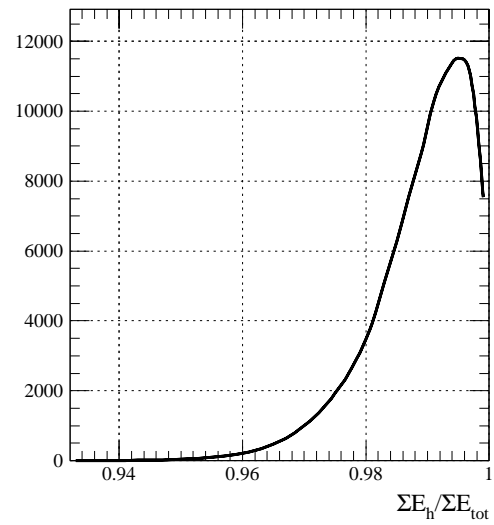CASTOR is designed to measure the hadronic and photonic contents of an interaction (both photon and charged particle multiplicity and energy) and identify the deeply penetrating hadrons, in an event-by-event mode, in the very forward phase space, $4.5 \leq \eta \leq 6.2$, corresponding to $0.23° \leq \theta \leq 1.27°$. Figure 3.1 shows the position of CASTOR in the ALICE experiment and Table 3-1 gives the dimensions and distances (Z) from the interaction point of the various sub-detectors. Figure 3.2 shows schematically the sub-detector elements of CASTOR.

The choice and design of some of the detectors follow closely similar ones proposed for current SPS and future LHC experiments. We will thus benefit from the ongoing and future R&D and the experience accumulated by these studies.

Table 3-1

Approximate dimensions of CASTOR for $4.5 \leq \eta \leq 6.2$. Projection on the plane perpendicular to the beam. For the calorimeter inclined at $45°$, the actual size is also shown by $\Delta(R'_{out} - R'_{in})$. Dimensions in mm.

Detector	Z	R_{in}	R_{out}	$\Delta(R_{out} - R_{in})$	$\Delta(R'_{out} - R'_{in})$
FCPMD	10595	43.0	235.4	192.4	
FPHMD	$\langle 10630 \rangle$	43.1	236.2	193.1	
CALORIMETER:					
EM (front)	10700	43.4	237.7	194.3	292.8
EM (back)	10767	43.7	239.2	195.5	294.6
H (front)	10767	43.7	239.2	195.5	294.6
H (back)	11525	46.8	256.1	209.3	315.4

3.1   Forward Charged Particle Multiplicity Detector

The purpose of the Forward Charged Particle Multiplicity Detector (FCPMD) is to measure $dN_{ch}/d\eta$ of the hadronic component of the interaction in the pseudorapidity range $4.5 \leq \eta \leq 6.2$.

Possible detector types to be considered are the Silicon Multipad Detector (SMD), which is an option for the seven FMDs of ALICE [ALICE Technical Proposal, Chapter 7, Section 7.2 (TP–7.2)]. For our multiplicity detector, fast timing is not a prerequisite. The detector is an annular disc, constructed in two half-rings for positioning around the beam pipe. The multiplicity will be unfolded from the total charge collected in the individual pads, using the known single-particle detector response function. A silicon pixel detector is also an option to be considered. The particulars of construction, support and electronics of the FCPMD will depend on the type finally chosen for the ALICE FMDs.
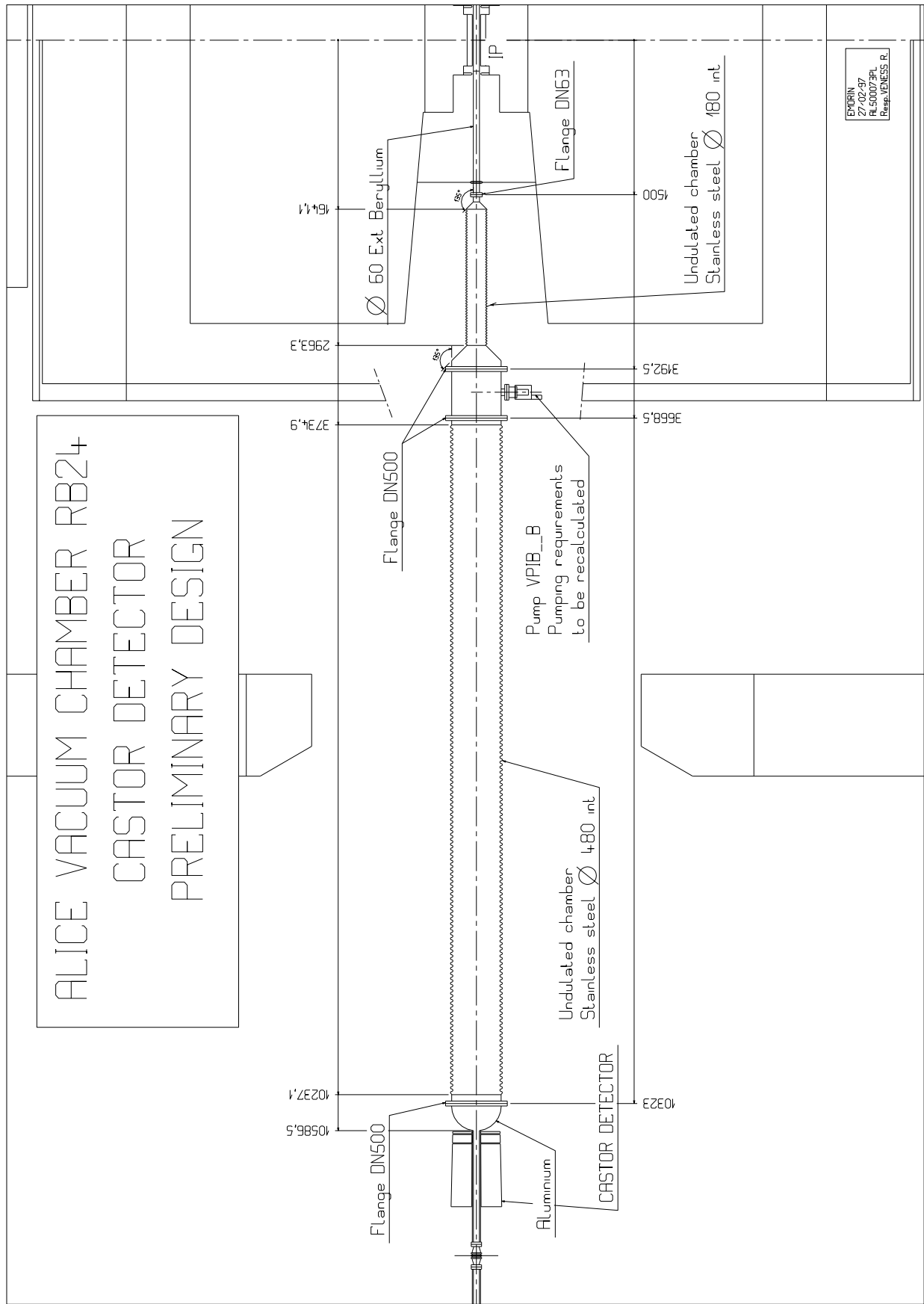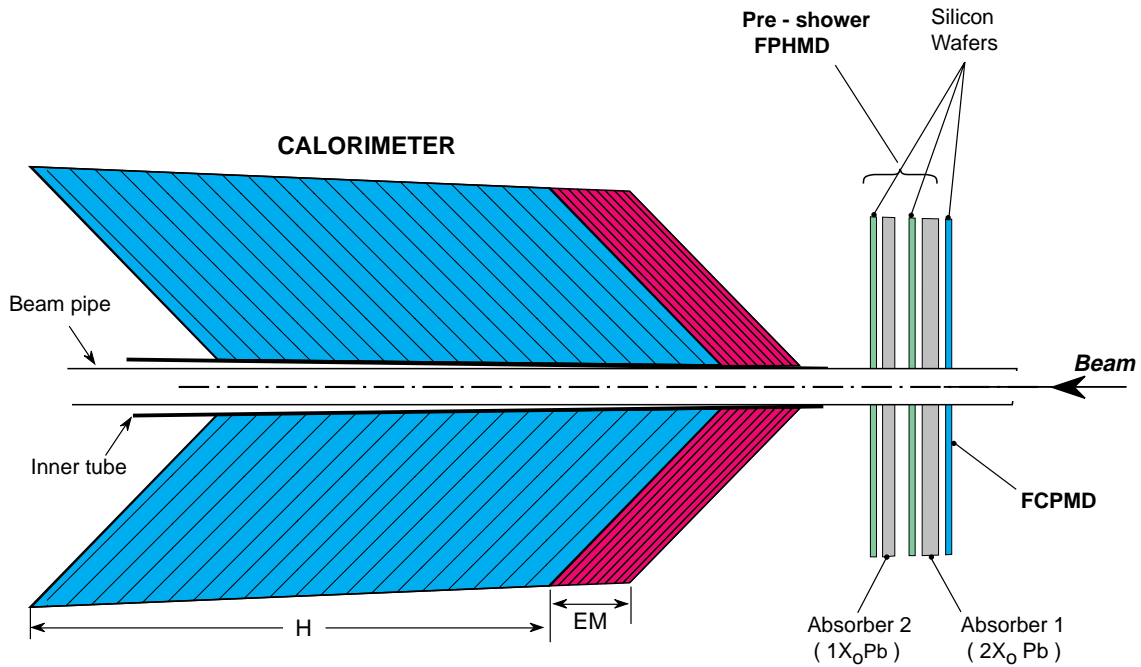
16

Figure 3.1: Position of CASTOR.

Figure 3.2: Schematic representation of the sub-detector elements of CASTOR.

3.2 Forward Photon Multiplicity Detector

The purpose of the Forward Photon Multiplicity Detector (FPHMD) is to measure the photonic component of the interaction, $dN\gamma/d\eta$ ($4.5 \leq \eta \leq 6.2$).

There are several studies of photon multiplicity detectors [13–15]. A possible design, a pre-shower type detector, uses silicon as the radiation-sensitive medium (CMS, RD36 [15]). For higher resolution and efficiency, the FPHMD will consist of two planes of Pb converter ($2 \, X_0$ and $1 \, X_0$), each followed by one active plane (silicon) (Fig. 3.2). The detector will be in the form of annular discs, constructed in two half-rings for positioning around the beam pipe. The read-out electronics, developed by RD36 [15], could be adopted for both the FCPMD and FPHMD (see also CERN–PPE/96–57).

For both the FCPMD and FPHMD, the radiation damage to silicon and associated electronics, especially when running p–p, needs to be addressed. There are solutions, however, such as using low-resistivity silicon (1–1.5 kΩ cm) cooled to about 5–10°C.

To count the number of photons and charged particles, a clustering algorithm will be used to identify hits in the FPHMD. Hadrons will be rejected by applying a threshold equivalent to about 2 MIPs on the total cluster pulse height. Hadrons not excluded by this cut will be identified and rejected by the veto detector sitting just in front. The FCPMD will also be used as a charged particle veto for the FPHMD. The employment of a veto detector allows a lower pulse-height cut to reject charged particles, which improves the

photon detection efficiency ($> 80\%$ for central events). In addition, the systematic error in estimating the number of photons should considerably decrease, because of event-by-event subtraction of the background.

Knowing both the charged particle and photon multiplicities event-by-event, we can obtain the ratio $N_{ch}/N\gamma$ and search for deviations from the normal value given by event generators in the range $4.5 \leq \eta \leq 6.2$. A characteristic signature of a Centauro event is the absence (or strong reduction) of the photonic component, giving a large value to this ratio.

3.3 Calorimeter

We shall employ an EM-H calorimeter to measure the total energy flux into the pseudorapidity range $4.5 \leq \eta \leq 6.2$. We want also to observe the development, intensity (energy content) and propagation of hadronic cascades as a function of the calorimeter depth (range of impinging hadrons), in order to identify any unusually penetrating component, as observed in hadron-rich cosmic-ray events. To meet this requirement, the calorimeter must be sampled along its length, with appropriate sampling steps corresponding to < 4 c.u. (1 c.u. = 1 X_0).

The limited space due to the beam pipe restricts the maximum pseudorapidity to $\eta \leq 6.2$. This necessitates the use of high-density absorber material for the calorimeter to reduce the transverse spread of the shower. The proposed calorimeter will be made of annular absorber discs, subdivided into octants, alternated with planes of active medium, which will read the energy at each reading plane. The absorber will be tungsten alloy (Triamet: 97% W, d = 17.2 g/cm³, X_0 = 3.64 mm, λ_I = 100 mm). The active medium, sandwiched between the W-absorber, will be quartz fibres (QF), to make use of the Cherenkov light produced by the traversing particles [16–18].

The advantages of using QF in this calorimeter are numerous:

- High-purity quartz is one of the most radiation-hard substances. Fused silica fibres with fluorinated fused silica cladding, irradiated at doses exceeding 20 Mgy (2 Grad), show no measurable sign of deterioration [19]. Such radiation hardness is more than adequate for the calorimeter for many more than ten years.
- The calorimeter is sensitive only to relativistic charged particles (practically, $\beta \geq 0.99$), which corresponds to 3.1 MeV electrons, 643 MeV muons and 850 MeV pions. It is insensitive to low-energy (MeV) neutrons, as well as to the effects of induced radioactivity.
- The sensitive depth needed for full containment of a hadron shower is considerably smaller than that required by a conventional dE/dx calorimeter [20].
- A QF calorimeter with 45° orientation to the impinging particle works as a 'shower-core' detector, sampling mostly the hadronic part of the shower, which lies effectively within a cone of $\sim \pm 10°$ in the direction of the particle. Thus, the energy of a hadronic shower can be reliably measured very close to the calorimeter's edge. The transverse profile of the hadron shower (~ 7 mm at 200 GeV) is considerably narrower than that measured by dE/dx conventional calorimeters, by a factor of ~ 3 for 90% containment [18, 19].
- $\beta \geq 0.99$ particles have constant light yield per unit length of trajectory and the total charged path length in a shower increases with energy.
- The calorimeter is very fast (~ 15 ns total). The production of Cherenkov light is an instantaneous process and timing tails resulting from shower thermalization are absent.

19

3.3.1 Calorimeter specifications

The W and QF sampling planes are arranged at $\sim 45°$ to the incoming particles for maximum Cherenkov light production and minimum lateral spread of the shower. The effective thickness of the tungsten absorber in the H-section is 14.1 mm, corresponding to 3.9 c.u. This thickness is sufficient to observe the outline of the cascades of the very penetrating particles and to follow their propagation through the length of the calorimeter (depth ~ 214 c.u.). Cosmic-ray detectors sampled the showers at every 1.8–3.5 c.u. and had a depth of 120–210 c.u. The total effective length of the calorimeter (7.8 λ_I) is also sufficient to contain fully the shower of a hadron (nucleon) impinging on it with $E_{mx} \sim 250$ GeV. Table 3-2 gives the calorimeter specifications.

Table 3-2
Calorimeter specifications

	Electromagnetic	Hadronic
Material	Tungsten + Quartz Fibre	Tungsten + Quartz Fibre
Disc:	$\langle R_{in} \rangle = 43.5$ mm, $\langle R_{out} \rangle = 338.5$ mm	$\langle R_{in} \rangle = 45.3$ mm, $\langle R_{out} \rangle = 350$ mm
	Thickness = 5 mm	Thickness = 10 mm
(at 45°)	Effective thickness = 7.07 mm	Effective thickness = 14.1 mm
No. discs	10	50
Eff. length	70.7 mm = 19.4 X_0 = 0.71 λ_I	707.1 mm = 7.07 λ_I
Quartz Fibre	~ 0.45 mm	~ 0.45 mm
No. QF planes	2	4
Sampling	1.94 X_0 ($X_0 \sim 3.64$ mm)	0.14 λ_I ($\lambda_I \sim 100$ mm)
Reading	1.94 X_0	0.14 λ_I
No. Readings	10	50
No. Channels	$10 \times 8 = 80$	$50 \times 8 = 400$
QF/W vol.	10%	10%

3.3.2 Mechanical construction and support

The tungsten-QF calorimeter is constructed in two half-cylinders for positioning around the beam pipe. Each half will besupported by a set of four 'legs', carrying its weight of approximately 600 kg, balancing it and moving it laterally on wheels. This support should also present the minimum possible mass, in order to reduce the background.

The W-absorber octants of the EM- and H-sections will be braced or screwed, at a 45° inclination, onto the two halves of an inner tube, made of 5 mm thick Fe and running the entire length of the calorimeter (Fig. 3.3. This tube constitutes the 'spine' of the calorimeter. The side supports, attached to each half-tube at the 45° position, prevent
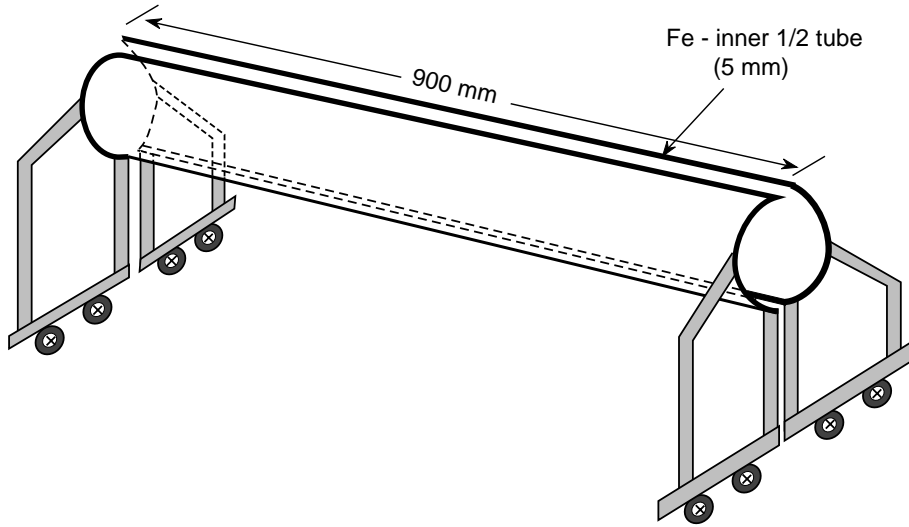
20

also the calorimeter from falling over.

Figure 3.3: Schematic representation of the mechanical construction and support for CAS-TOR.

3.3.3 Radial segmentation of active medium

To ensure uniformity of response as a function of pseudorapidity, each active plane contains a number of fibres which is progressively increased as a function of the radius R, keeping the ratio QF/W volume constant. There are 11 such radial 'segmentations', corresponding to $\Delta\eta = 0.2$ for the five inner rings and 0.1 for the outer six. Table 3-3 gives the details of the radial segmentation of the average sampling plane of the EM calorimeter, using QF of external diameter 0.45 mm. The number of QFs at each radial segmentation, N_{QF}^i, is given by

$$N_{QF}^i = (V_{QF}/V_W)(x_W/d_{QF}^2)(1/n)(R_{out}' + R_{in}')|_i \qquad (6)$$

where V_{QF}/V_W is the design volume ratio, x_W/d_{QF}^2 is the thickness ratio of the W-absorber to the QF single plane, n is the number of QF planes and R_{out}', R_{in}' are the true outer and inner radii of the octant at each segmentation.

The choice of tungsten for absorber with small λ_I (10 cm compared with 15 cm for Cu) reduces the quantity of QF for the same QF/absorber volume (filling ratio). For the EM calorimeter with absorber plane thickness d = 5 mm, a filling ratio $V_{QF}/V_W = 1/10$ is satisfied using two single-fibre planes. For the H-section with absorber thickness of 10 mm, we need to employ four QF planes. The two or four single-fibre planes produce a uniform lateral (or ϕ) active-medium distribution and make the calorimeter insensitive to changes in the shower profile, as they improve the sampling of showers in their early stage of development, where the core is extremely narrow and dense. This should result in the diminishing of the constant term in the energy resolution.

The average length of QF amounts to $\sim$ 560 m per single-fibre plane and the total length for the entire calorimeter is about 123 km.

Table 3-3

Number of QFs per octant for each pseudorapidity segmentation for the average sampling plane of the EM-section (n = 2, OD fibre = 0.45 mm).

Pseudorapidity	R'_{in} (mm)	R'_{out} (mm)	N_{QF}
6.1–5.9	48.4	83.2	81
5.9–5.7	83.2	101.6	114 (+33)
5.7–5.5	101.6	124.1	139 (+35)
5.5–5.3	124.1	151.5	170 (+31)
5.3–5.1	151.5	185.1	208 (+38)
5.1–5.0	185.1	204.6	240 (+32)
5.0–4.9	204.6	226.1	266 (+26)
4.9–4.8	226.1	250.1	295 (+29)
4.8–4.7	250.1	276.1	325 (+30)
4.7–4.6	276.1	305.2	359 (+34)
4.6–4.5	305.2	337.3	397 (+38)

3.3.4 Read-out

For more efficient light collection and for higher spatial resolution in ϕ, the QF annular plane (and the absorber) are divided into octants. The QFs of each octant will be read by a PMT with quartz window to allow the detection of the UV photons, which constitute about two-thirds of the photon spectrum [21]. We shall also investigate the possibility of using HPD [22]. The light from the QF will travel to the PMT through an air light-guide, made of lightweight, stiff plastic (Polymicro) and painted with UV-reflecting paint (Fig. 3.4). The air light-guide homogenizes the response of the different parts of the photocathode to different fibres. This solution avoids the necessity for sharp bending-back of the QFs to reduce the production of Cherenkov light from particles outside the detector. It is also inexpensive and easy to construct. The read-out of the calorimeter necessitates in total 480 PMTs and electronic channels.

3.3.5 Energy resolution

There is a wealth of tests and data for QF calorimeters [16–21, 23]. For our purpose, we modelled the calorimeter in a simple way to include its essential features. Figure 3.5 shows the resolution, $\sigma(E)/E$, as a function of the QF/W volume ratio for the H-section, for pions and gammas. For the proposed QF/W $\sim 1/10$, we find resolutions of about 10% and 7% for pions of 100 and 250 GeV, respectively. Finer sampling does not improve the resolution significantly. For gammas, the corresponding resolutions are 3.5% and 3%. We conclude that the chosen QF/W ratio is adequate. The test of a prototype with different V_{QF}/V_W ratios and detailed Monte Carlo simulations will be necessary for determining the cost-effective QF/W value.
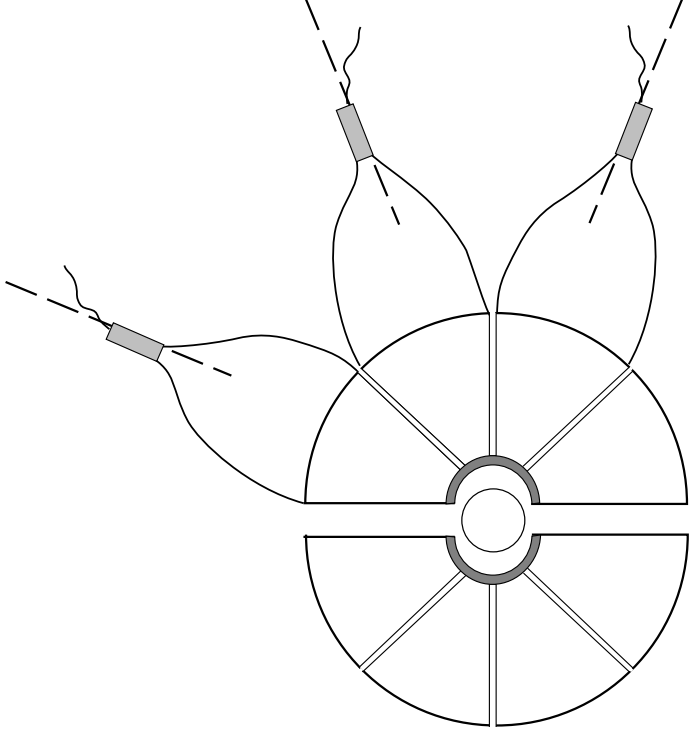
Figure 3.4: Schematic representation of the light-guide assembly for the CASTOR calorimeter.

3.3.6 Energy calibration and resolution measurements

The energy calibration and resolution measurements of the EM- and H-sections of the calorimeter will be done in two stages:

- Individual sampling unit (absorber + QF planes) gain equalization.

- Entire EM-, H-section energy calibration and resolution measurement.

The energy calibration will be accomplished by using MIPs, such as muons. MIPs transverse the entire length of the calorimeter and deposit the same amount of energy per sampling unit. Although this energy is small, its equivalent visible energy is substantially larger, permitting the calibration of the calorimeter [18].

The energy resolution will be studied using different hadron beams and energies, as well as electrons. Because of the modularity of the construction, the energy resolution can be studied for different QF/W filling ratios. A small prototype calorimeter will be built and studied in the spirit of the study described in reference [18].

To check the stability of each PMT and the signal amplitude of each sampling unit (light reduction because of radiation damage to the QFs), a laser system will be used. It will shine light onto the photocathode directly and also through the longest QF of the plane.
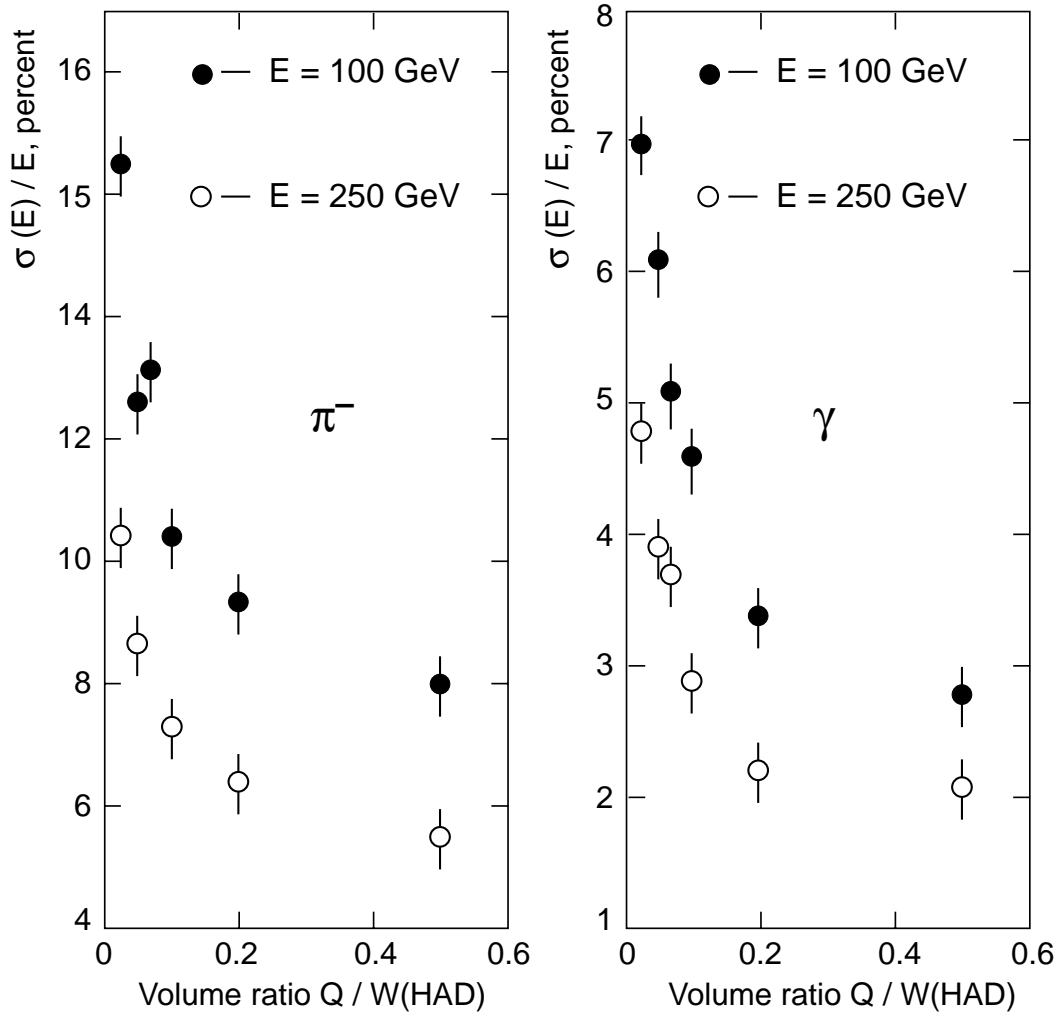
Figure 3.5: Energy resolution of the CASTOR calorimeter hadronic section as a function of the QF/W volume ratio for pions and photons and for incident energies of 100 GeV and 250 GeV.

4 GENERAL CONSIDERATIONS

4.1 Beam induced background

Beam–gas interactions (for a detailed treatment see TP–8.7).

Since the event vertex is determined to within a few cm, we need to consider only random coincidences between a true event and a downstream beam–gas interaction.

CASTOR consists of detectors with very short memory time and presents a very small area to the background particles (silicon detectors: $\tau \sim 2\ \mu s$, A ~ 0.1 m^2; calorimeter: $\tau \sim 15$ ns, A ~ 0.5 m^2). In addition, the EM/H calorimeter with QF planes at $\sim 45°$ orientation to the interaction point is sensitive only to particles originating from the event-vertex side. Particles entering the calorimeter from the rear side produce a signal attenuated by at least a factor of 50 [18]. This limits the beam–gas interactions to within a length of ~ 10 m. Furthermore, the use of the correlated information on the beam–beam collision, obtained from the two ZDCs on either side of the event vertex, will help minimize the background from beam–gas interactions. Therefore this source of background should cause no problem.

Beam losses

Local beam losses in any of the machine elements, or beam misdirecting and diffused beam-halo are potentially dangerous sources of background and high radiation to very forward detectors. This is a matter which needs to be examined together with the small angle absorber, designed to protect the low-beta quadrupoles.

QED electron pairs

This is a background consisting of electrons produced in the interaction at small angles to the beam and with very small transverse momenta, unique to very high-energy heavy-ion colliding beams. However, the number of QED electrons reaching CASTOR (Z ~ 10 m) should be negligible (see TP–8.7).
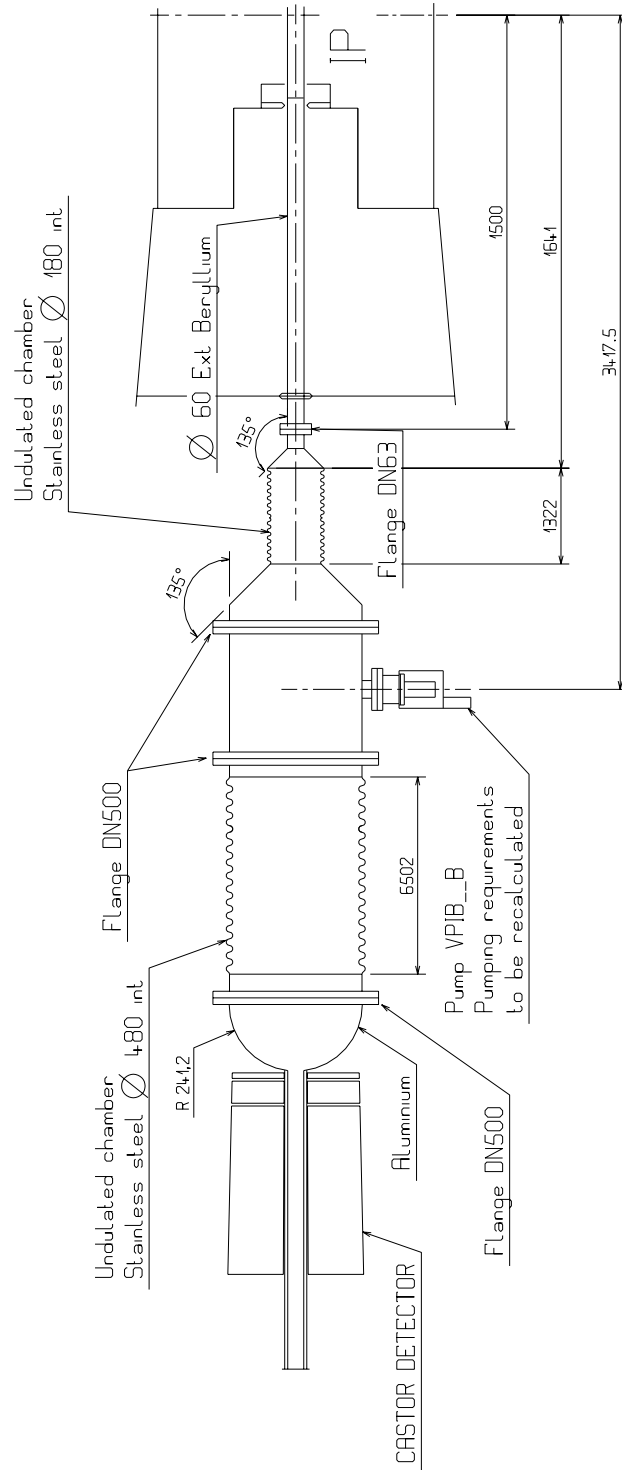
4.2 Vacuum-pipe-related background

The very forward position ($0.23° \leq \theta \leq 1.27°$) occupied by CASTOR causes the particles emitted from the interaction vertex into $4.5 \leq \eta \leq 6.2$ to transverse a considerable thickness of material of the conventional ($\phi \sim 120$ mm) beam pipe, thus creating an exceedingly large number of secondary particles.

To avoid this catastrophic background, an 'enlarged diameter' corrugated beam pipe was designed, enclosing the pseudorapidity of interest ($4 \leq \eta$) (Fig. 4.1). GEANT calculations were carried out for such a (stepped) vacuum chamber, considering all material due to flanges, vacuum pumps, chamber supports, etc. Particles emitted from the interaction vertex and directed within a cone of half-angle $6°$, corresponding to $\eta \sim 3$, were allowed to decay and interact with the surrounding material. Figures 4.2 and 4.3 show the total charged particle and photon multiplicity density distributions seen at the FCPMD and FPHMD respectively. Figures 4-4 and 4-5 show the point of origin along z of charged particles and photons seen at the FCPMD and FPHMD and produced away from the interaction vertex. Note that the signal (corresponding to particles coming from the interaction vertex) has been suppressed in these last two figures.

The noise to signal ratio is below 30% for both charged particles and photons. It will increase minimally when all surrounding material is incorporated, such as the calorimeter support and the ALICE magnet sides. It will still remain, however, of the order of 30% for charged particles and 25% for photons, which is acceptable for the 'identification' of a Centauro or mini-Centauro event (see discussion in Section 5).

ALICE VACUUM CHAMBER RB24
CASTOR DETECTOR
PRELIMINARY DESIGN
NOT TO SCALE

Undulated chamber
Stainless steel ⌀ 180 int

⌀ 60 Ext Beryllium

135°

Flange DN63

Undulated chamber
Stainless steel ⌀ 480 int

R 242

Aluminium

Flange DN500

CASTOR DETECTOR

Flange DN500

Pump VPIB_B
Pumping requirements
to be recalculated

135°

IP

1500

1641

3417.5

1322

6502

Figure 4.1: Schematic representation of the vacuum beam pipe in front of CASTOR.

$1/2\pi R\ dN_{ch}/dR\ [\ 10^{-4}\ cm^{-2}\ ]$

R [10^{-3} cm]
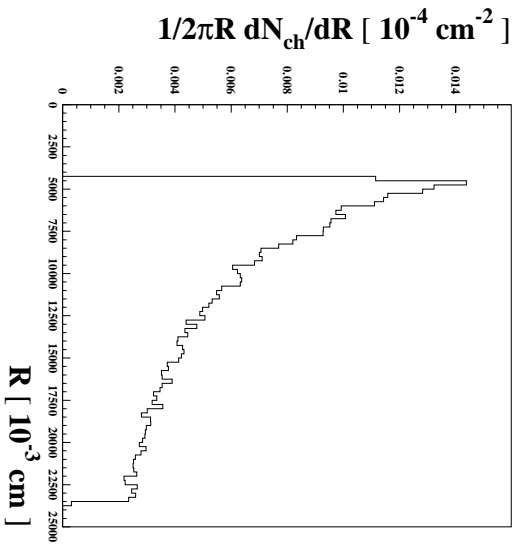
Figure 4.2: Charged particle density distribution on FCPMD, obtained from 10 central HIJING events.

$1/2\pi R\ dN_{ph}/dR\ [\ 10^{-4}\ cm^{-2}\ ]$

R [10^{-3} cm]
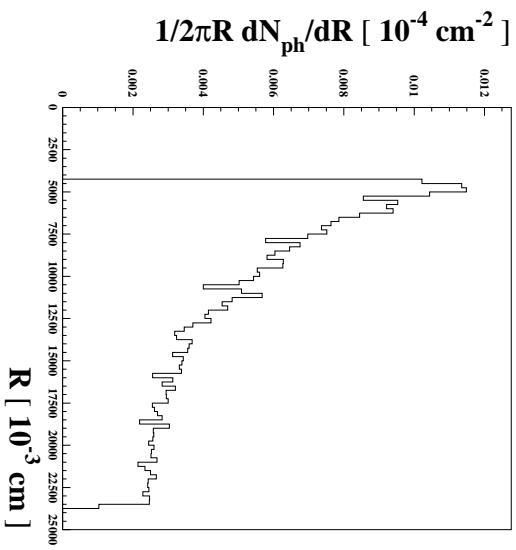
Figure 4.3: Photon density distribution on FPHMD, obtained from 10 central HIJING events.
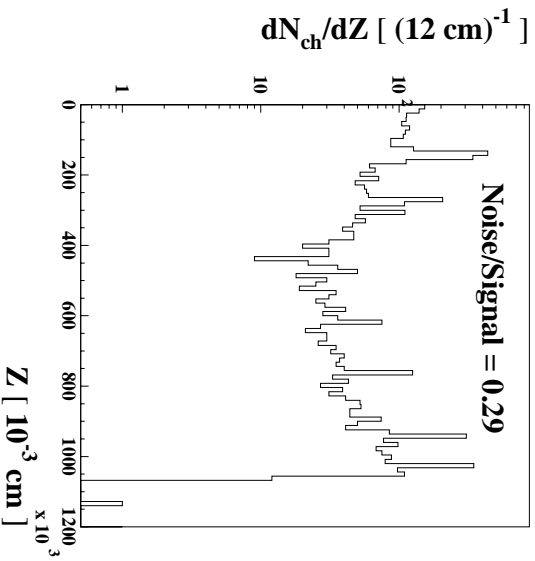
$dN_{ch}/dZ\ [\ (12\ cm)^{-1}\ ]$

Noise/Signal = 0.29

Z [10^{-3} cm]

Figure 4.4: Z position of origin of charged particles seen by the FCPMD, obtained from 10 central HIJING events.

$dN_{ph}/dZ\ [\ (12\ cm)^{-1}\ ]$

Noise/Signal = 0.25

Z [10^{-3} cm]
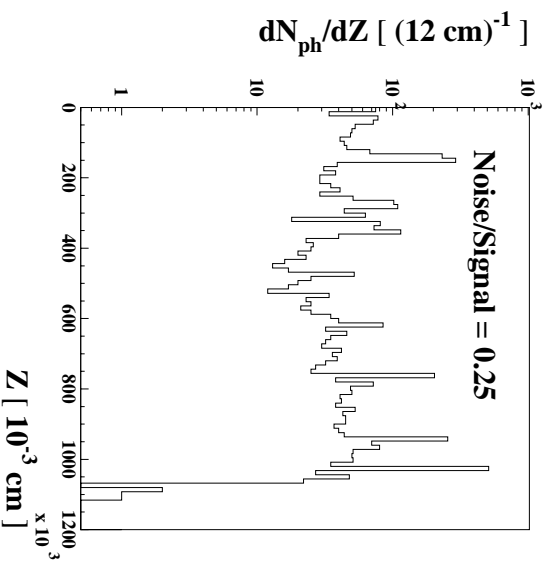
Figure 4.5: Z position of origin of photons seen by the FPHMD, obtained from 10 central HIJING events.

5 TRIGGER FOR CENTAURO EVENT AND STRANGELET

5.1 Online trigger

The Centauro events and strangelets will be searched for offline in an event-by-event mode. Therefore one needs an appropriate online trigger to minimize the uninteresting data recorded, without, however, imposing unwanted constraints and biases.

The first-level online trigger will be accomplished by the ZDCs of ALICE. We select very central events ($< 15\%$ of interactions) in order to maximize the overlap of the colliding nuclei and the number of participant nucleons.

The second-level offline trigger will be enforced by the multiplicity and the calorimeter detectors:
- Multiplicity detectors: (a) $N_\gamma/N_h << 1$,
                                          (b) N_h small (< 200) (for a Centauro event).
- Calorimeter: (a) $\Sigma E_\gamma/\Sigma E_h << 0.3$ (for a Centauro event),
                                            (b) Non-uniform energy deposition on octants of the last
                                               few reading planes of the hadronic section
                                               (for a very penetrating object, 'strangelet').

5.2 Identification of Centauro-type event

We have examined the possibility of identifying Centauro-type events with the CASTOR sub-detectors, by calculating with GEANT the ratios, E_{em}/E_{had} and N_γ/N_{ch} for normal hadronic and Centauro-type events (50 HIJING events). We have included the decays of the primary produced particles and their interactions with the surrounding matter of the beam pipe, but not the detector resolution. Table 5-1 gives these ratios in the rapidity range $4.5 \leq y \leq 6.2$. The first and second entries correspond to 'pure' hadronic (Fig. 5.1 and 5.2) and Centauro events, respectively. The third and fourth entries correspond to 'mixed' events, where we have allowed the production of about equal numbers of $(\pi^+ + \pi^-)$ and baryons (I) (Fig. 5.3 and 5.4) and $1.33 \times (\pi^+ + \pi^-)$ as baryons (II)

<div align="center">

Table 5-1

GEANT calculations of the ratios E_{em}/E_{had} and N_γ/N_{ch} for hadronic
and Centauro-type events.

Event Type	E_{em}/E_{had}	N_γ/N_{ch}
'Pure' hadronic	0.34 ± 0.022	0.82 ± 0.034
'Pure' Centauro	0.002 ± 0.003	0.07 ± 0.09
'Mixed' I	0.13 ± 0.040	0.64 ± 0.12
'Mixed' II	0.16 ± 0.037	0.69 ± 0.13

</div>

We observe that a 'pure' Centauro event is unequivocally identified. 'Mixed' events can also be identified, but the amount of mixing admitted will depend on the detector resolution. The combination of the two measurements, multiplicity and energy, will greatly improve the identification.
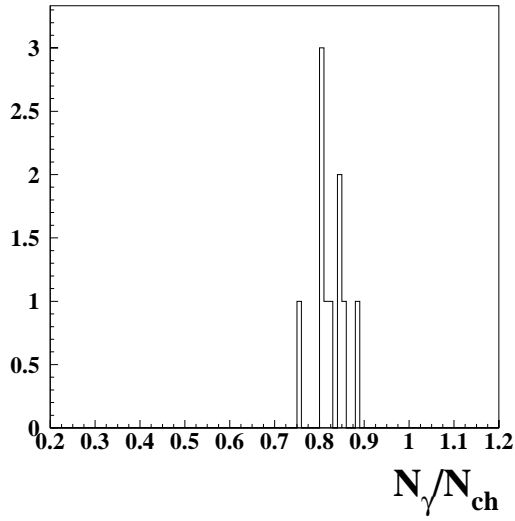
Figure 5.1: N_γ/N_{ch} for pure hadronic events, obtained from 10 central HIJING events.
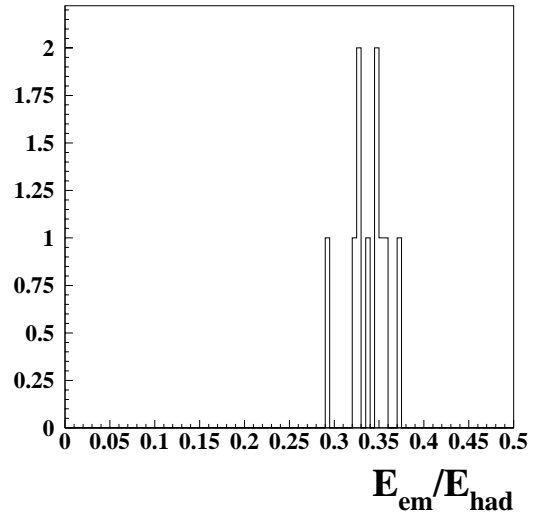

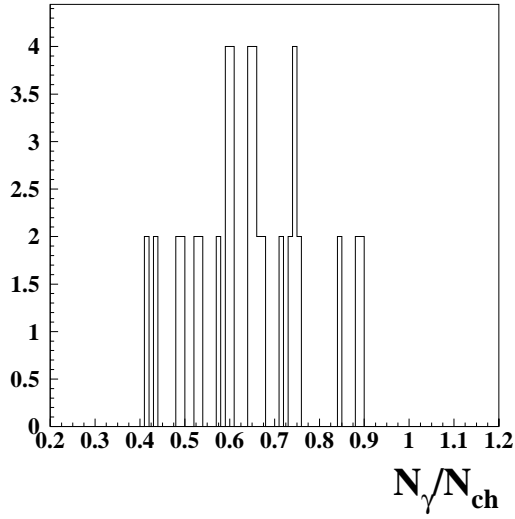Figure 5.2: E_{em}/E_{had} for pure hadronic events, obtained from 10 central HIJING events.

Figure 5.3: N_γ/N_{ch} for mixed events comprising about the same number of $(\pi^+ + \pi^-)$ as baryons, obtained from 50 central HIJING events.

Figure 5.4: E_{em}/E_{had} for mixed events comprising about the same number of $(\pi^+ + \pi^-)$ as baryons, obtained from 50 central HIJING events.

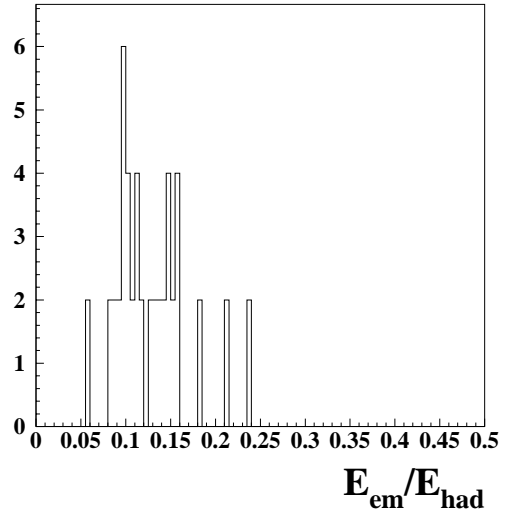## 5.3 Identification of strangelet (long-penetrating component)

The strongly penetrating component could be observed in the CASTOR calorimeter via three characteristic signatures:

– The strong concentration of energy, limited to a very narrow sector of the calorimeter,

– a transition cascade curve, with a structure of many maxima,

– very slow attenuation of the transition cascades.

We have simulated the passage of strangelets (stable, metastable and unstable) through the calorimeter [33] and, generally, these features appear in the simulated events. The typical transition curve of the cascade developing in the W-absorber of the calorimeter, produced by an unstable strangelet with A_{str}=15, is shown in Fig. 5.5.

Some points should, however, be mentioned:

– The longitudinal structure and the separation of consecutive humps in the transition curve depends on the mass of the strangelet, being much better for lighter strangelets.

– On the other hand the massive strangelet, which carries a larger amount of energy, gives the stronger signal, more easily seen above the background.

The typical background expected to be produced by nucleons coming from the Centauro fireball decay is shown in Fig. 5.6. It should be distributed rather uniformly over the whole calorimeter volume, in contrast to the signal produced by a strangelet, which is expected to be limited to a very narrow sector of the calorimeter. Thus, it seems that the signal-to-background ratio will be acceptable in the case of division of the calorimeter into 8 or more sectors.
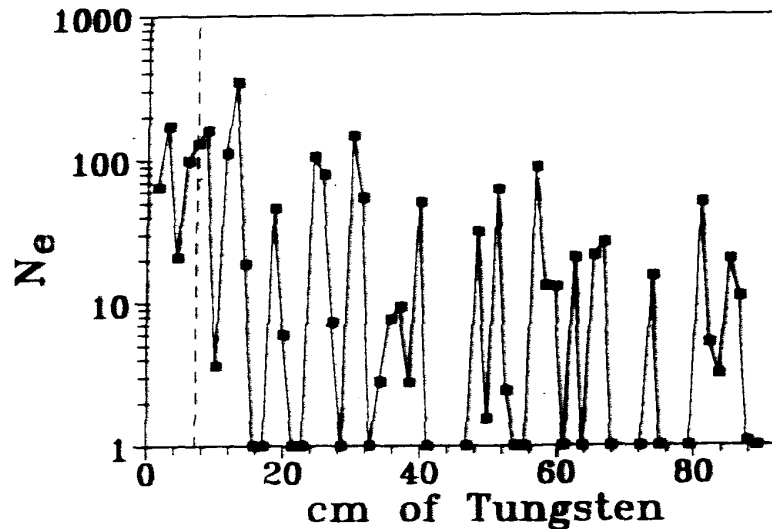

Figure 5.5: Example of simulated transition curve produced by an unstable strangelet (A_{str}=15), penetrating through one sector (out of 10) of the CASTOR calorimeter.
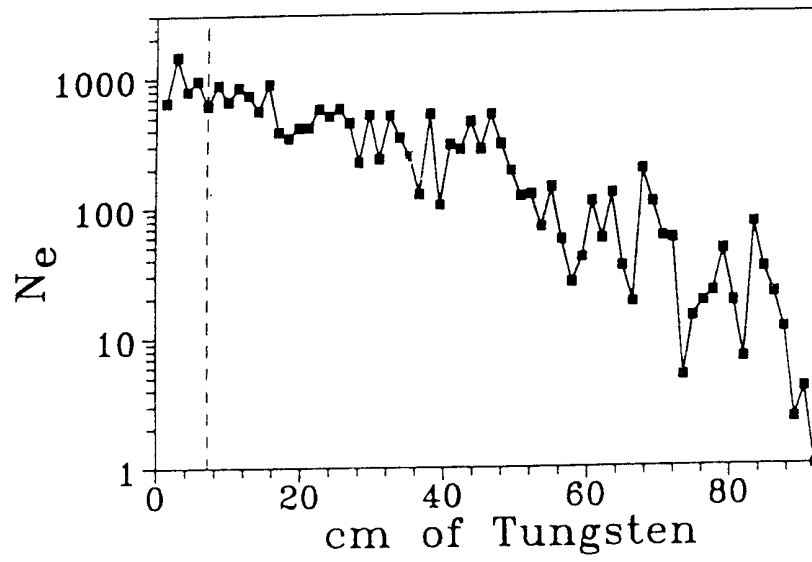
Figure 5.6: Typical 'background' produced by the Centauro decay hadrons in all 10 sectors of the CASTOR calorimeter.

6   COST ESTIMATE

An approximate cost estimate of the CASTOR detector system is given in Table 6-1. It uses current prices for all items, some of which could become cheaper in the years to come.

<div align="center">

Table 6-1

Cost estimate of CASTOR components

</div>

FCPMD			
(see TP–13.1)			$\sim$ 110 kCHF
FPHMD			
(see TP–13.1)			$\sim$ 220 kCHF
CALORIMETER			
Quartz fibres:	$\sim 123\ 000 \times 2.0$ CHF/m	$\sim$	250 kCHF
Light guides:		$\sim$	20 kCHF
Tungsten:		$\sim$	100 kCHF
Electronic channels:	$\sim 480 \times 1$ kCHF/channel	$\sim$	480 kCHF
Mechanical support:		$\sim$	20 kCHF

<div align="center">

TOTAL $\sim$ 1200 kCHF

</div>

The Institutes, which are participating in the CASTOR detector, are:

- Athens, University of.
- "Demokritos", Institute of Nuclear Physics.
- Ioannina, University of.
- Krakow, Institute of Nuclear Physics.
- Moscow, Institute for Nuclear Research.
- Protvino, Institute for High Energy Physics.

Appendix I. Super Heavy Particles

The total energy in the centre-of-mass system for $Pb + Pb$ collisions at LHC is about 1150 TeV. Therefore, the unique possibility could be considered to produce Super Heavy Particles (SHPs) by nucleus–nucleus collisions, with masses much larger than the centre-of-mass energy in proton–proton collisions. However, at present no theory predicts the existence of particles with masses of several tens of TeV. On the contrary, a 'gauge desert' is proposed in the Standard Model for masses in the range 100 GeV–10^{12} TeV.

In more advanced studies the search for new vector bosons was investigated [24] by proposing to use the beams of future large hadron colliders. Since no theoretical estimates of their masses could be made, the possibility to detect new heavy vector bosons $V^{\pm}, V^0$ was discussed for masses up to 6 TeV, at the centre-of-mass energies of colliders up to 14 TeV. Obviously, for the estimation of production cross-sections one needs to use a modified version of the Standard Model, such as the Extended Gauge or Strong Interaction Higgs Model [25, 26]. If these new heavy vector bosons exist, they could be observed in proton–proton collisions.

In principle, SHPs with masses larger than the centre-of-mass energy of nucleon–nucleon colliders could be produced in the subthreshold processes by nucleus–nucleus collisions. However, to calculate the production cross-section one should take into account the collective phenomena with the participation of several multi-nucleon or multi-quark interactions.

The phenomenological parton model was proposed [27] to estimate the probability of observation of SHPs in ion–ion collisions at LHC. This model was successfully applied to the subthreshold and near-threshold production of kaons and antiprotons in proton–nucleus and nucleus–nucleus collisions [28]. It was observed that production cross-sections could be expressed as a universal function of generalized scaling quark–parton parameters, such as the Bjorken scaling parameter X, but in this case different in incident (Z) and in target (X) nuclei. Values of Z and X larger than 1 arise to provide the production of particles at subthreshold energies for nucleon–nucleon processes. This scaling was observed for different quark flavours. Therefore, one may expect that the model could be applied to heavier unknown quarks and the collective phenomena could be due to some space–time properties of nucleus–nucleus interactions or to the universal structure function of the nucleus.

An extrapolation of scaling dependence to larger masses and to the collision energy up to 2.77 TeV/nucleon and for the expected luminosity, gives optimistic results. For $Pb + Pb$ collisions more than 10 SHPs per year for the mass of 35 TeV would be produced, if they exist. The production cross-section increases exponentially for lower masses [29].

The method of SHP detection depends on whether the particles are stable or long-lived, or they promptly decay to some lighter particles of the same nature. The latter decay branch leads to the lightest final particles, which do not interact with simple hadrons possibly because of different quantum numbers and their conservation. The possible methods for SHP detection in this type of decay could be similar to those proposed for the identification of supersymmetrical particles [30]. The first is a multijet search accompanied by large missing transverse energy. The second method is the detection of same-sign dileptons with a large number of jets and large missing transverse energy. These search possibilities are provided by the central detector of ALICE. The problem of background is considered in reference [30]. If SHPs represented the new neutral-gauge bosons mentioned above [24], the leptonic decay to electron-neutrino could give a signature of the SHP production

process. However the sensitivity of the central detector for a measurement of large mass decays should be further investigated. A different detection method could be proposed for the stable or long-lived SHP search.

Because of the large mass of SHPs and strong suppression of subthreshold particle production for high transverse momenta, these particles should be produced at small angles to the beam axis at large rapidity. Even with the possible subtraction of the missing energy of the light final decay particles, the signal from hadronic or electromagnetic calorimeters should greatly exceed the amplitudes produced by hadron and electromagnetic cascades of lower mass particles. However, since the velocity of SHPs is sometimes assumed to be rather small [31], as little as one per cent of the velocity of light, it is necessary to measure the time-of-flight of the SHPs at large rapidities. This could be done on a flight path of about 10 m from the collision point to the CASTOR installation. The time resolution could be quite moderate and the start time would be determined by the ALICE Forward Multiplicity Detector [32].

Acknowledgements

References

[1] Proposal 'Maximum acceptance detector for the Fermilab collider', 1992.

[2] C.M.G. Lates, Y. Fugimito and S. Hasegawa, Phys. Rep. **65** (1980) 151;
A.S. Borisov et al., Phys. Lett. **B190** (1987) 226.

[3] Pamir Collaboration, Proc. 20th International Cosmic Ray Conference, Moscow, USSR, 1987, ed. V.A. Kozyarivsky et al., (Nauka, Moscow, 1987) pp. 334, 351, and 383;
S. Yamashita, A. Ohsawa and J.A. Chinellato, Proc. International Symposium Cosmic Rays and Particle Physics, Tokyo, Japan, 1984, ed. A. Ohsawa and T. Yuda (Institute for Cosmic Ray Research, Tokyo, 1984) p. 30;
H. Tamada, **24**th ICRC, Rome, (1995) vol. 1, p. 236.

[4] K. Goulianos, Commun. Nucl. Part. Phys. **17**, 195 (1987).

[5] K. Kang and A. White, Phys. Rev. **D42** (1990) 835.

[6] A.D. Panagiotou, A. Karabarbounis, A. Petridis, Z. Phys. **A333** (1989) 355;
A.D. Panagiotou, A. Petridis, M. Vassiliou, Phys. Rev. **D45** (1992) 3134;
M.N. Asprouli, A.D. Panagiotou, E. Gladysz-Dziadus, Astropart. Phys. **2** (1994) 167;
E. Gladysz-Dziadus and A.D. Panagiotou, Proc. International Symposium on Strangeness & Quark Matter, Krete, 1–5 September 1994, eds. G. Vassiliadis, A.D. Panagiotou, B.S. Kumar, J. Madsen (World Scientific, Singapore, 1995) p. 265;
E. Gladysz-Dziadus and A.D. Panagiotou, ALICE–Note/PHY # 18, 1995.

[7] A.D. Panagiotou, G. Mavromanolakis, J. Tzoulis, UA/NPPD–26–95 (1995);
Proc. Conf. on "Strangeness in Hadronic Matter", Budapest, 15-17 May 1996, Heavy Ion Phys. **4** (1996) 347;

[8] C. Greiner, D.H. Rischke, H. Stocker and P. Koch, Phys. Rev. **D38** (1988) 2797.

[9] C. Greiner, H. Stocker, UFTP–258/1991;
H.J. Crawford, M.S. Desai, G.L. Shaw, Phys. Rev. **D45** (1992) 857.

[10] Z. Buja et al., Proc. 17th International Cosmic Ray Conference, Paris, 1981, Vol. 11, p. 104.

[11] T. Arisawa et al., Nucl. Phys. **B424** (1994) 241.

[12] E. Gladysz-Dziadus, Y.V. Kharlov, A.D. Panagiotou, S.A. Sadovsky, ALICE-Note/Physics 97-06.

[13] P. Aspell et al., CERN/DRDC/94–47 (1994).

[14] M.M. Aggarwal et al., VECC/EXP/95–02 (1995); ALICE/95–20 (1995).

[15] RD36, CMS Technical Proposal for the LHC, CERN/DRDC/94–47 (1994).

[16] O. Ganel, R. Wigmans, SSC Note SDC–93/575 (1993).

[17] G. Anzivino et al., Nucl. Instrum. Methods **A357** (1995) 380.

[18] P. Gorodetsky et al., Nucl. Instrum. Methods **A361** (1995) 161.

[19] A. Contin et al., CERN/DRDC/94–4 (1994);
E. Chiavassa et al., ALICE/95–11 (1995).

[20] R. Wigmans, CMS TN/94–304 (1994).

[21] A. Contin et al., Nucl. Instrum. Methods **A357** (1995) 369.

[22] R. DeSalvo et al., Nucl. Instrum. Methods **A315** (1992) 375;
H. Arnaudon et al., Nucl. Instrum. Methods **A342** (1994) 558.

[23] RD40, CERN/LHCC/95–27 (1995).

[24] G. Altarelli et al., Z. Phys. **C45** (1989) 109.

[25] P. Ramond, Annu. Rev. Nucl. Part. Sci. **33** (1983) 31.

[26] W.B. Lee et al., Phys. Rev. **D16** (1977) 1519.

[27] A.B. Kurepin, ALICE/93–03, Internal Note/PHY (1993).

[28] A.I. Berlev et al., Proc. 'Quarks '88', May 1988, Tbilisi (World Scientific, Singapore, 1989), p. 679.

[29] A.B. Kurepin, ALICE/95–47, Internal Note/PHY (1995).

[30] ATLAS Collaboration, Technical proposal for the LHC, CERN/LHCC/94-43 (1994).

[31] T. Hemmick et al., Phys. Rev. **D41** (1990) 2074.

[32] ALICE Collaboration, Technical proposal for the LHC, CERN/LHCC/95–71 (1995).

[33] E. Gladysz-Dziadus and Z. Wlodarczyk, ALICE-Note (in preparation).

[34] E. Witten, Phys. Rev. **D30** (1984) 272;
M.S. Berger and R.L. Jaffe, Phys. Rev. **C35** (1987) 213;
S.A. Chin and A.K. Kernan, Phys. Rev. Lett. **43** (1979) 1292.

[35] G. Wilk and Z. Wlodarczyk, J. Phys. **G22** (1996) L105.